

Special Issue Research Article

Establishing a Robust and Reliable Response from a Potent Osmium-Based Photosensitizer *Via* Lipid Nanoformulation[†]

Houston D. Cole¹, Menitte Eroy², John A. Roque III¹, Ge Shi¹, Mina Guirguis², John Fakhry², Colin G. Cameron*¹, Girgis Obaid*² and Sherri A. McFarland*¹

Received 15 September 2022, accepted 4 December 2022, DOI: 10.1111/php.13756

ABSTRACT

Osmium (Os) based photosensitizers (PSs) are a unique class of nontetrapyrrolic metal-containing PSs that absorb red light. We recently reported a highly potent Os(II) PS, rac-[Os (phen)₂(IP-4T)](Cl)₂, referred to as ML18J03 herein, with light EC₅₀ values as low as 20 pm. ML18J03 also exhibits low dark toxicity and submicromolar light EC₅₀ values in hypoxia in some cell lines. However, owing to its longer oligothiophene chain, ML18,J03 is not completely water soluble and forms 1-2 µm sized aggregates in PBS containing 1% DMSO. This aggregation causes variability in PDT efficacy between assays and thus unreliable and irreproducible reports of in vitro activity. To that end, we utilized PEGmodified DPPC liposomes (138 nm diameter) and DSPEmPEG₂₀₀₀ micelles (10.2 nm diameter) as lipid nanoformulation vehicles to mitigate aggregation of ML18J03 and found that the spectroscopic properties important to biological activity were maintained or improved. Importantly, the lipid formulations decreased the interassay variance between the EC₅₀ values by almost 20-fold, with respect to the unformulated ML18J03 when using broadband visible light excitation (P = 0.0276). Herein, lipid formulations are presented as reliable platforms for more accurate in vitro photocytotoxicity quantification for PSs prone to aggregation (such as ML18J03) and will be useful for assessing their in vivo PDT effects.

INTRODUCTION

Photodynamic therapy (PDT) is a light activated treatment modality that typically harnesses an excited photosensitizer (PS) molecule and molecular oxygen to elicit phototoxicity (1). PDT is used clinically for a number of cancer and noncancer indications, including antimicrobial therapy, dermal treatments and the treatment of age-related macular degeneration. Unlike systemic therapies, PDT benefits from spatiotemporal control over tissue damage

whereby phototoxicity is confined to regions of both PS accumulation and light irradiation. PDT also has the capacity to convert weakly immunogenic tumors into strongly immunogenic ones, under specific conditions. In doing so, PDT increases tumor infiltration of cytotoxic T cells, even in lesions that have not been treated (2–4), and has shown evidence of the abscopal effect in patients when combined with immune checkpoint therapy (5).

The classes of PSs that are currently used in the clinic are generally derived from tetrapyrroles (*e.g.* porphyrins, chlorins, and phthalocyanines) that require oxygen for their phototherapeutic activity. In an effort to design systems with improved properties, metal-based PSs have emerged.

Our major efforts in this area have been aimed at exploiting alternate modes of action for treating hypoxic tumors (6-9), creating immunomodulating metallodrug PSs (10-12), and translating such PSs to the clinic (13,14). Our TLD1433, a ruthenium (Ru)-based coordination complex, is the first nontetrapyrrolic metal-containing PS to enter human clinical trials for cancer PDT (ClinicalTrials.gov Identifiers: NCT03945162, NCT03053635). This PS is activated by green light and is being developed to treat nonmuscle invasive bladder cancer (NMIBC) in patients that have failed frontline therapy (13,14). TLD1433, with the formula rac-[Ru(4,4'-dmb)₂(IP-3T)](Cl)₂, is a bisheteroleptic Ru(II) polypyridyl complex whereby the central Ru (II) ion is coordinated to two 4,4'-dimethyl-2,2'-bipyridyl (4,4'dmb) ligands and an imidazo[4,5-f][1,10]phenanthroline (IP) ligand tethered to a-terthiophene (3T). Ru PSs such as TLD1433 can simultaneously exploit highly photoreactive triplet intraligand charge transfer (³ILCT) excited states for therapy and emissive triplet metal-to-ligand charge transfer (3MLCT) excited states for imaging. The prolonged lifetimes of the ³ILCT states give rise to high singlet oxygen (¹O₂) quantum yields and alternate modes of action involving the redox-active oligothiophene unit.

We recently extended this concept to related osmium (Os)-based PSs of the type rac-[Os(LL)₂(IP-4T)](Cl)₂, where LL = [1,10] phenanthroline (phen), 2,2'-bipyridine (bpy) or 4,4'-dmb and 4T = α -quaterterthiophene (6,7). For a given set of ligands, Os(II) offers the opportunity to shift the absorption to longer wavelengths (15) while maintaining high quantum yields for triplet state formation and $^{1}O_{2}$ generation. For example, rac-[Os(phen)₂(IP-4T)](Cl)₂ (ML18J03, Fig. 1) has a longest-wavelength absorption maximum in the red near 655 nm (ε _{655 nm} = 3715 $^{-1}$ cm $^{-1}$) and a $^{1}O_{2}$

¹Department of Chemistry and Biochemistry, University of Texas at Arlington, Arlington, TX

²Department of Bioengineering, University of Texas at Dallas, Richardson, TX

^{*}Corresponding authors email: colin.cameron@uta.edu (Colin G. Cameron), email: girgis.obaid@utdallas.edu (Girgis Obaid), email: sherri.mcfarland@uta.edu (Sherri A. McFarland).

[†]This article is part of a Special Issue celebrating the 50th Anniversary of the American Society for Photobiology.

^{© 2022} American Society for Photobiology.

quantum yield of 95% (6). These photophysical characteristics result in light-triggered cytotoxicity toward cancer cells with normoxic EC_{50} values near 10 nm for 633-nm red light and as low as 20 pm for broadband visible light under our conditions (100 J cm⁻² delivered at a rate of 20 mW cm⁻²). The low dark toxicity associated with ML18J03 gives rise to phototherapeutic indices (PIs) as large as >10⁶ with broadband visible light and still almost 10^4 with red light. In hypoxia, the wavelength-dependence for photocytotoxicity disappears, and the EC_{50} values are submicromolar with PIs around 10^2 .

At the time they were reported in 2020, the potencies documented for this Os PS class were unprecedented (for both normoxia and hypoxia). We recently reported Ru PSs that surpass these values, but these systems are not active with red light (8.9). Thus, ML18J03 and its close relatives remain (to our knowledge), the most potent systems with therapeutic red light under both oxygen conditions. In addition, they are well tolerated in vivo, with maximum tolerated doses (MTD) over 200 mg kg⁻¹. However, their aqueous solubilities could be improved as longer oligothiophene chains such as 4T are prone to aggregation. Such intermolecular associations appear to reduce potency. The effect is most pronounced in the submicromolar regime and can result in EC50 values and PIs that vary over several orders of magnitude between assays. We hypothesized that lipid nanoformulations of ML18J03 could reduce selfassociation and improve aqueous solubility and thus provide a more robust and reliable response for advancing this promising PS class.

Liposomes are the predominant lipid formulations used for hydrophobic or amphiphilic therapeutic agents that have been approved for clinic use over the past three decades. For PDT specifically, liposomal formulations have also been leveraged to increase the aqueous solubility of hydrophobic PSs, thereby improving their pharmacokinetic profiles and their therapeutic efficacy (16). A noteworthy example is Visudyne, an FDAapproved liposomal nanoformulation of the PS benzoporphyrin derivative (BPD) that has been clinically approved to treat Wet Age-Related Macular Degeneration (AMD) since 2000 (17). Important preclinical liposomal formulations that are currently under investigation include two nanoformulations of the PS meta-tetra(hydroxyphenyl)chlorin (mTHPC), Foslip® and Fospeg®, the latter exploiting a long-circulating PEG coating (18). Both lipid formulations Foslip® and Fospeg® have been shown to improve the in vitro activity and in vivo therapeutic efficacy of mTHPC with respect to Foscan® (19,20), an approved ethanol/PEG₄₀₀/water solution of the same PS.

Aside from liposomes, micellar formulations have also been shown to offer improved aqueous solubility of hydrophobic PSs and increase their circulation half-lives (21–23). One advantage of micelles (<50 nm) over liposomes (80–200 nm) is their relatively small hydrodynamic diameter. The smaller diameters of micelles minimizes clearance by the reticuloendothelial system and favors homogenous intratumoral distribution (24–26). However, the lower stability of micelles in serum can result in reduced overall accumulation of therapeutic payloads in solid tumors (relative to liposomes) (27,28).

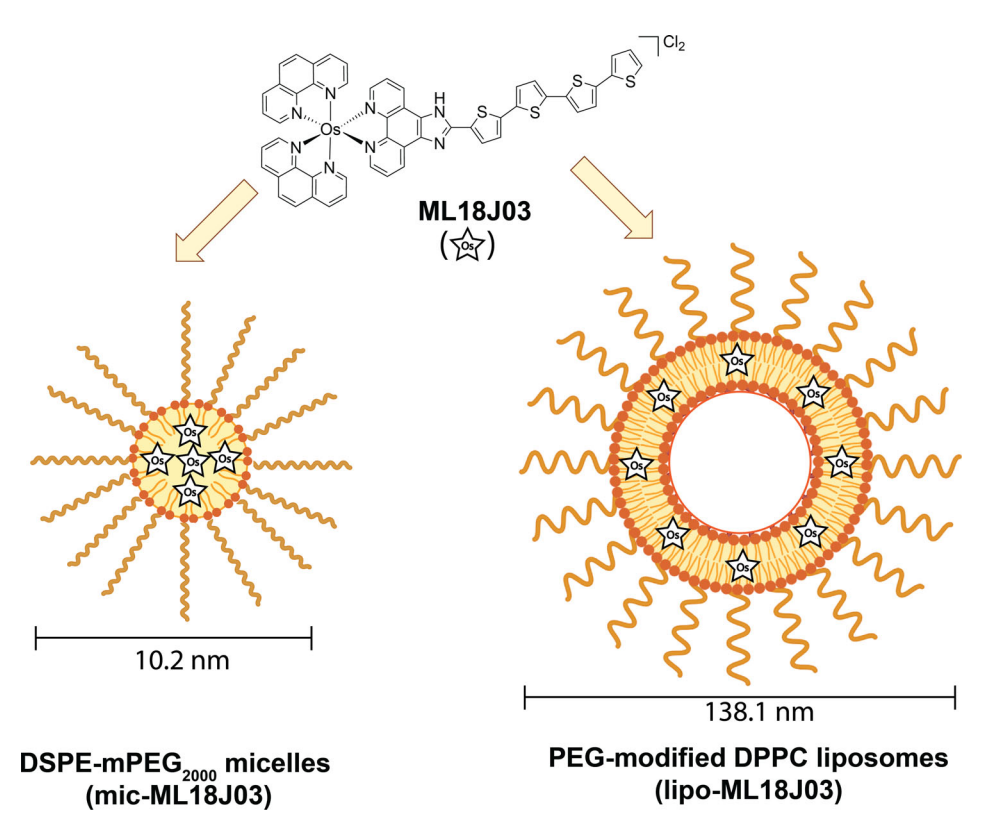


Figure 1. Chemical structure of the Os-based PS rac-[Os(phen)₂(IP-4T)](Cl)₂ (ML18J03) and graphical representations of its respective lipid formulations, DSPE-mPEG₂₀₀₀ micelles (mic-ML18J03) and PEG-modified DPPC liposomes (lipo-ML18J03). Lipid formulations are not drawn to scale. Figure prepared using an academic license of Biorender.

In addition to improving the pharmacokinetics and aqueous solubility of hydrophobic PSs, we and others have shown that lipid formulations can also serve as multifunctional platforms for molecular targeted agent delivery. This enables molecular tumor specificity, which is achieved by surface modification with one or more tumor-specific ligands, which has been repeatedly shown to improve the efficacy and safety of PDT (29). Furthermore, lipid formulations can provide unparalleled opportunities for phototriggered multi-agent delivery, which offers unprecedented synergistic antitumor effects at significantly de-escalated dosages of otherwise toxic anticancer agents (30,31). We have previously demonstrated that tethering various hydrophobic and hydrophilic PS molecules to the lipid bilayer modulates the release kinetics of entrapped agents from liposomes (32). In this context, liposomes are thus particularly attractive due to their large aqueous core that can encapsulate more than 10⁴ drug molecules per liposome, in addition to the lipid bilayer that entraps hydrophobic PS agents.

In prior studies, we demonstrated that both PEG-modified liposomes and micelles are capable of encapsulating the hydrophobic PS BPD as well as various hydrophobic lipid conjugates of BPD (33). These formulations prevented aggregation of the BPD variants in aqueous environments and retained their fluorescence emission by up to 86%. This retention of fluorescence emission also positively correlated with their ability to generate $^{1}O_{2}$ upon photoexcitation (P < 0.05). Furthermore, PEGmodified DPPC liposomes and DSPE-mPEG micelles prevented leakage of PS molecules into serum for up to 24 h with 37°C incubation.

The clinical relevance of liposomal and micellar formulations of PSs and the numerous advantages they both offer for PDTbased combination regimens motivated the assessment of PEGmodified liposomal and micellar formulations of ML18J03 in this study. The primary goal was to improve the aqueous solubility and physical stability of ML18J03 in biological environments. To that end, the PEG-modified DPPC liposomes and DSPEmPEG micelle lipid formulations of ML18J03 (Fig. 1) are intended to reduce the interassay variability of activity that can confound the reproducibility and reliability of assessing such hydrophobic PS. Furthermore, these strategies to physically stabilize ML18J03 in aqueous environments, including serum, lay the foundation for future work where lipid formulations will serve as clinically relevant vehicles for in vivo PDT, with superior pharmacokinetic profiles and controlled aggregation profiles. These approaches will ultimately provide more predictable serum pharmacokinetics, tumor uptake kinetics, and tumor distribution profiles that promise to increase the robustness and consistency of antitumor responses.

MATERIALS AND METHODS

Unless otherwise specified, reagents and solvents were purchased commercially and used without further purification. Water for biological experiments was deionized to a resistivity $\geq 18.2 \text{ M}\Omega$ using either a Barnstead or Milli-Q® filtration system and autoclaved for sterilization. Buffers were adjusted to precise pH against a two-point calibrated VWR^{\otimes} B10P pH meter (pH_{ref.} = 4.00, 7.00; Fisher Science Education, S25849A/B). Cellular assays were carried out in 384 well plates as previously described (9,12). Free ML18J03 was prepared at 25 mm in DMSO and diluted with $1\times$ Dulbecco's Phosphate-Buffered Saline (DPBS) without Ca^{2+} or Mg^{2+} (diluted and sterile filtered from $10\times$ DPBS, Corning 20-031-CV) for cellular assays (6). Formulated ML18J03 was diluted directly in DPBS, and the highest concentration of formulated ML18J03 tested was ≤50 μM (since the formulations were < 200 µm in ML18J03). In addition, two different dilution methods for free ML18J03 were compared using two distinct serially diluted series: (a) 1×10^{-12} to 300 μ m and (b) 5×10^{-4} to 300 μ m. For this pipette tips were exchanged more frequently than what is done in our standard assay condition (6): tips in set (a) were exchanged at 0.1 nm, and tips in set (b) were exchanged at 30 µm and between each dilution below 600 nm.

Nanoformulation in liposomes and micelles. Synthesis of liposomal and micellular formulations. Liposomal formulations of ML18J03 were prepared by a thin film hydration method (33). All lipids were purchased from Avanti Polar Lipids unless otherwise stated. Briefly, 0.2 µmol of ML18J03 (methanol; 0.6 molar percentage composition, (mol%)) were added to chloroform solutions of 23.5 µmol 1,2-dipalmitoyl-sn-glycero-3phosphocholine (DPPC), 10.5 µmol cholesterol and 1 µmol 1,2distearoyl-sn-glycero-3-phosphoethanolamine-N-[methoxy(polyethylene glycol)-2000] (DSPE-mPEG₂₀₀₀). Chloroform was evaporated from the mixtures using nitrogen gas flow and the lipid films were hydrated with 1 mL sterile 1× DPBS (Corning) at 42°C in a water bath for 30 min. The hydrated films were then subject to 20 min of continuous vortexing, followed by sonication (Fisher 20 kHz Model 120 Sonic Dismembrator) using 20 s on/40 s off cycles at 42°C for 1 h. Samples were then extruded 11 times at 42°C using 100 nm polycarbonate membranes (Whatman). For calculation of entrapment efficiencies, liposomes were synthesized as described and doped with an additional 0.018 µmol of lipid anchored fluorophore 1,2-dipalmitoyl-sn-glycero-3phosphoethanolamine-N-(lissamine rhodamine B sulfonyl) (16:0 Liss Rhod PE). Following liposome synthesis, unentrapped ML18J03 that was not removed by extrusion was removed by Sepharose CL-4B (Sigma) size-exclusion chromatography equilibrated with sterile 1× DPBS. Concentrations of entrapped ML18J03 were measured using UV-Visible absorption spectrophotometry ($\varepsilon_{436} = 6.2 \times 10^4 \text{ m}^{-1} \text{ cm}^{-1}$ in acetonitrile (6)) with respect to the concentration of the lipid anchored fluorophore 16:0 Liss Rhod PE ($\varepsilon_{566} = 9.5 \times 10^4 \text{ m}^{-1} \text{ cm}^{-1} \text{ in DMSO}$).

Micellular formulations of ML18J03 were prepared using DSPEmPEG₂₀₀₀ with varied mol% compositions of ML18J03 according to adaptations of previously published protocols (33,34). Briefly, 0.71 µmol of DSPE-mPEG₂₀₀₀ (2805.5 g mol⁻¹; NOF America Corporation) in chloroform was mixed with ML18J03 (methanol solutions) at the following mol% compositions: 10.7, 15.2, 26.4, 37.5, 45.6, 54.5, 64.2 and 70.6. The mixtures were homogenized using an ultrasonic water bath for 1 min at room temperature, after which the solvent mixtures were evaporated using nitrogen gas flow. The residue containing DSPE-mPEG2000 and ML18J03 was then hydrated in 1 mL sterile 1× DPBS and heated to 50°C in a water bath for 1 h, followed by 5 min sonication in an ultrasonic water bath for 5 min. After cooling to room temperature, the hydrated lipid mixture was subject to sonication (Fisher 20 kHz Model 120 Sonic Dismembrator) using 20 s on/40 s off cycles at 42°C for 1 h. Upon cooling once again to room temperature, unentrapped insoluble ML18J03 was removed from the micellular solution by filtration using 0.22 µm polyethersulfone filters (MilliporeSigma). Concentrations of entrapped ML18J03 were measured as described above.

Physical characterization. The entrapment efficiencies of ML18J03 in liposomal and micellular formulations were calculated as follows:

Entrapment efficiency =

$$\frac{\text{mol ML18J03 retained after purification}}{\text{mol ML18J03 doped into liposomes or micelles}} \times 100\% \quad (1)$$

Liposomal and micellular ML18J03 formulations were physically characterized using a Zetasizer Pro (Malvern). For hydrodynamic diameter measurements, 2 µL of nanoconstructs were diluted in 1 mL sterile 1× DPBS and measured in triplicate by dynamic light scattering. For ζpotential measurements, 10 µL of nanoconstructs were diluted in sterile 0.9% saline and measured in triplicate using gold electrode cells. For hydrodynamic diameter measurements of free ML18J03, a 1 mg mLsolution in DMSO was diluted 100-fold in PBS and measured immediately in triplicate using dynamic light scattering.

Spectroscopy. For the spectroscopic studies, liposomal and micellular ML18J03 formulations were prepared as described above and diluted in PBS to obtain 20 µm of ML18J03 equivalent. Free ML18J03 in methanol was also dried and dissolved in appropriate volumes of DMSO to obtain a final concertation of 20 µm of ML18J03 equivalent.

UV-visible spectroscopy. Electronic absorption spectra were recorded using a Jasco v730 spectrometer with 10 mm path length quartz cuvettes, using water in the reference beam. The liposomal formulation was slightly opaque, so a post-process correction was applied to compensate for background scatter.

Emission. Steady-state emission spectra were acquired in Ar-sparged PBS solution using a PTI QuantaMaster spectrometer equipped with a Hamamatsu R5509-42 NIR PMT (range \approx 600–1400 nm). The spectrometer internally corrected any wavelength-dependent nonlinearities in lamp output and detector sensitivities. The most intense, longest-wavelength peak in the excitation spectrum was chosen as $\lambda_{\rm ex}$.

Transient absorption. Differential excited state absorption (ESA) spectra and transient absorption (TA) lifetimes were measured on an Edinburgh Instruments LP-980 spectrometer with the PMT-LP detector. A Continuum Minilite Nd:YAG laser provided excitation pulses at 355 nm (\approx 0.25 Hz, \approx 5 ns pulse width, \approx 7–9 mJ per pulse). ESA spectra were acquired in 10 nm intervals, and TA lifetime was measured at a single wavelength, with the bandwidth optimized for maximum detector response.

Singlet oxygen. The quantum yield for singlet oxygen sensitization (Φ_{Δ}) was calculated from the baseline-corrected intensity of the $^{1}O_{2}$ emission band centered near 1276 nm using the actinometric method described by Eq. (2), where I denotes the emission integration, A is the UV–Vis absorption of the solution at the excitation wavelength, and η is the solvent's refractive index. $[\text{Ru}(\text{bpy})_{3}]^{2+}$ in MeCN ($\Phi_{\Delta}=0.56^{4}$) was used as the standard, indicated by the subscript S.

$$\Phi_{\Delta} = \Phi_{\Delta,S} \left(\frac{I}{I_S} \right) \left(\frac{A_S}{A} \right) \left(\frac{\eta^2}{\eta_S^2} \right) \tag{2}$$

RESULTS

Photobiology

We previously reported the dark and light in vitro activities of free ML18J03 against several cancer cell lines (6). Using the SKMEL28 human melanoma cell line as a representative example, ML18J03 is nontoxic in the dark with an average EC₅₀ value of around 60 µm under our standard assay conditions. This value is not significantly impacted by oxygenation status but can be higher or lower with variation of certain assay parameters (Fig. 2; Tables S1, S2). The in vitro photocytotoxicity associated with ML18J03 in 1% hypoxia is relatively consistent between assays and falls near 0.5-1 µM, giving rise to PI values on the order of 10² regardless of the visible light wavelength employed. However, the sub-µM photocytotoxicity measured for ML18J03 under normoxic conditions is subject to sizable variation between assays that becomes more pronounced with shorter wavelengths of light. The general trend is that the more potent the response, the larger this variability (Fig. 2; Table S1). Nevertheless, even the least potent EC50 value on this continuum falls within the nm regime and is still considered extremely potent. For instance, the EC₅₀ value for ML18J03 with broadband visible light (fluence = 100 J cm^{-2} , irradiance = 20 mW cm^{-2}), the most potent treatment condition, varies over three orders of magnitude (from 26.3 nm down to 17.8 pm). The corresponding PIs span from 10⁴ to well over 10⁶. The reason(s) behind this variability in sub-μΜ potency has not been definitively established, but PS aggregation is one consideration. ML18J03, along with a variety of other PSs derived from the π -expansive IP-4T ligand, tends to form a suspension with visible particulate that precipitates on the micropipette tips upon serial dilution. Consequently, the EC50 values extrapolated from the dose-response assay can be significantly impacted by the dilution protocol, especially in the sub-µm regime (Fig. 3; Tables S3 and S4).

Serial dilutions prepared without exchanging tips are subject to "carry-over" effects such that the PS doses are higher than their intended concentrations, whereas tip changes between each dilution results in PS doses that are lower than their intended concentrations. This issue preferentially affects the doses farther down the dilution series (*i.e.* the lowest doses). The inability to obtain doses that reflect their intended concentrations is compounded by the dynamic nature of aggregates and their nonuniformity within and across assays. Together, these factors lead to a large variation of EC₅₀ values in the sub-μm regime across assays.

Dynamic light scattering confirmed the presence of ML18J03 aggregates in PBS solution supplemented with 1% DMSO ([PS] = 0.85 μM , 10 $\mu\text{g mL}^{-1}$). Their diameters appeared to be in the 1.1–2.1 μm range (1.6 \pm 0.5 μm), with the caveat that sedimenting aggregates compromise the accuracy of such measurements. Based on the quantifiable presence of aggregates, we hypothesized that lipid formulation of ML18J03 might reduce such self-association and thus lead to a more robust and consistent in vitro PDT response in the sub- μm regime. Indeed, both micellar and liposomal formulations of ML18J03 produced solutions that left no visible residue on the micropipette tips and EC50 values independent of the dilution method.

The mean phototherapeutic efficacy of ML18J03 was maintained upon lipid formulation in either liposomes (lipo-ML18J03) or micelles (mic-ML18J03). Representative responses under the different light conditions are shown in Fig. 4 and also highlight that lipid formulation lowers the dark cytotoxicity. Importantly, the interassay variability was greatly reduced (Table S5). This is depicted in Fig. 5, where the min-max plots demonstrate the larger variability in EC50 values of unformulated, free ML18J03 regardless of which excitation wavelength is used. The pooled EC₅₀ values for all lipid formulations exhibited a statistically significant reduction in the interassay variance (5×10^6) with respect to the interassay variance of the free ML18J03 (8.9×10^5) in the case of broadband visible light excitation. For green and red light excitation, the variance was also lower in the case of the pooled EC50 values for the lipid formulations but not statistically significant (6.2-fold and 3.4-fold lower; P = 0.0607and P = 0.1965, respectively). The lack of significance with the longer wavelength datasets is likely attributed to the fact that both excitation conditions resulted in lower phototoxicity than the visible light excitation. It appears that the interassay variability is related to the potency of the PDT protocol applied, further emphasizing the importance of lipid formulation to mitigate interassay variability when evaluating novel potent metal-based sensitizers.

Nanoformulation

ML18J03 entrapment in liposomes and micelles. ML18J03 was entrapped within PEG-modified DPPC liposomes (lipo-ML18J03) at a PS mol% of 0.6 with respect to total lipid content. When higher amounts of hydrophobic PSs are entrapped, the lipid bilayer of liposomes can become prone to disruption that leads to their aggregation. As such, a PS mol% of 0.6 was used which we have previously shown not to impact liposome stability (33). The entrapment efficiency of the PS within lipo-ML18J03 was 93% (Table 1). ML18J03 was also entrapped in DSPE-mPEG₂₀₀₀ micelles (mic-ML18J03) at varying PS mol% values of 11, 15, 26, 38, 46, 55, 64 and 71 with respect to total formulation content. Micelles are typically more tolerant of

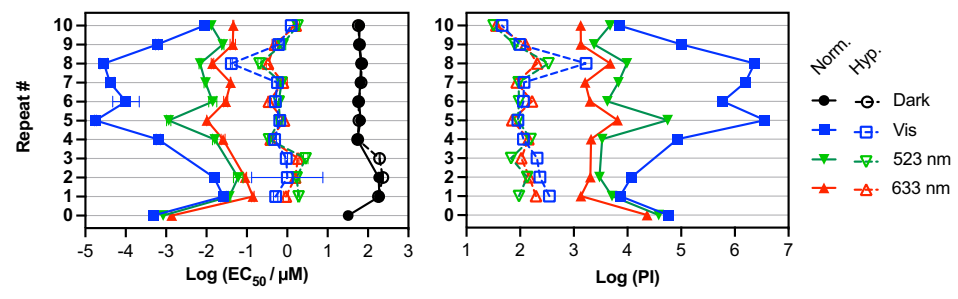


Figure 2. Longitudinal study of ML18J03 activity toward SK-MEL-28 human melanoma cells compared over 11 different assays, each performed in triplicate. Normoxic data points are represented by solid symbols, and hypoxic ($1\% O_2$) data are represented by open symbols (connecting lines used to guide the eye). Treatments were dark or light (fluence = 100 J cm^{-2} ; irradiance 20 mW cm^{-2}) with cool white visible, 523 nm green or 633 red LEDs. Note that the visible treatment is the most potent light condition due to contributions from the blue region of the spectrum.

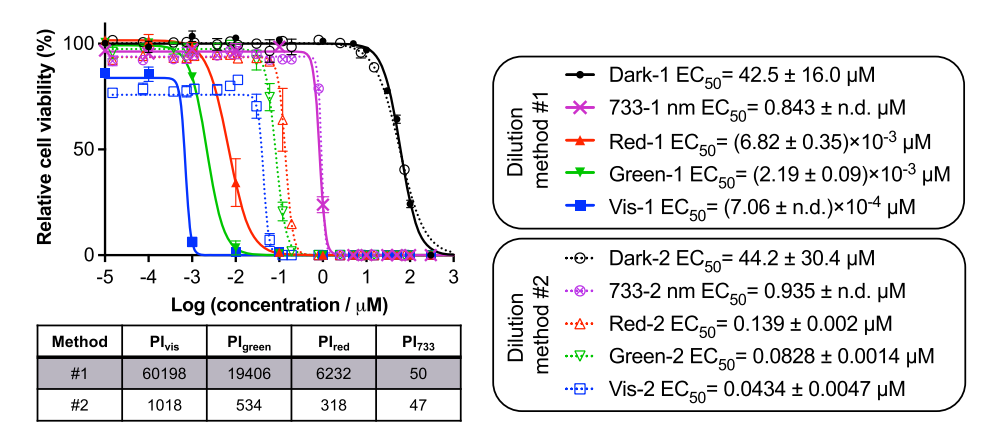


Figure 3. Comparison of activity toward SK-MEL-28 human melanoma cells using two different serial dilution methods for free ML18J03. Tips in dilution method #1 (solid symbols and lines) were exchanged only at 0.1 nm, whereas tips in dilution method #2 (open symbols and dotted lines) were exchanged at 30 μm and between each dilution below 600 nm. Differences in photocytotoxicities as a result of the two dilution methods only manifest for sub-μm EC_{50} values.

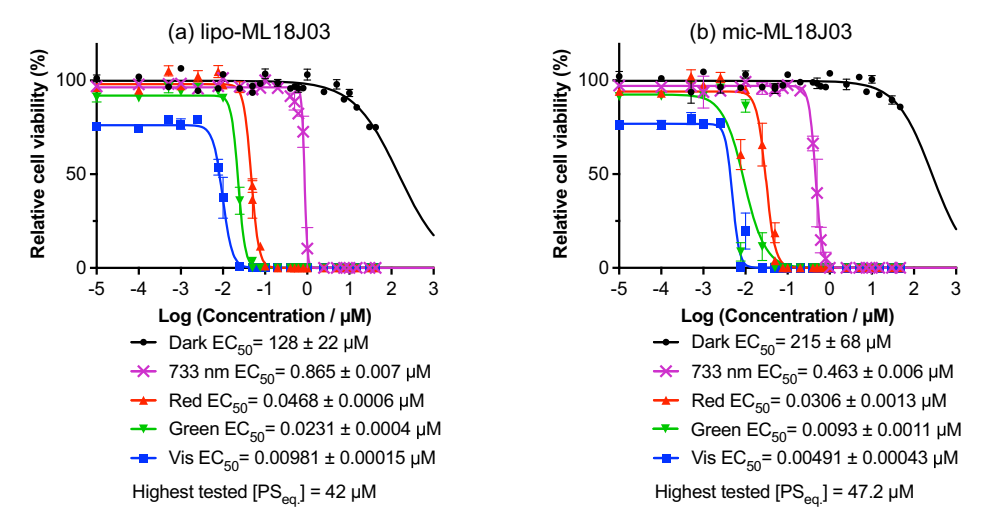


Figure 4. Dose–response (\pm SD) curves for SK-MEL-28 human melanoma cells treated with mic-ML18J03 at 11 mol% PS loading (a) or lipo-ML18J03 at 0.6 mol% PS loading (b) in normoxia. Treatments were dark (black filled circles) or light (fluence = 100 J cm⁻²; irradiance 20 mW cm⁻²) with cool white visible (blue squares), 523 nm (green inverted triangles), 633 nm (red triangles) or 733 nm (purple crosses). The irradiance for 733 nm was 5 mW cm⁻².

higher PS mol% entrapment, although PSs can experience lower entrapment efficiencies and significant static quenching when loaded in high quantities within micelles. As such, the range from 11 to 71 mol% was evaluated to determine this threshold. The entrapment efficiency of the PS within mic-ML18J03 was quantitative at the lowest PS loading (100% for the 11 mol%)

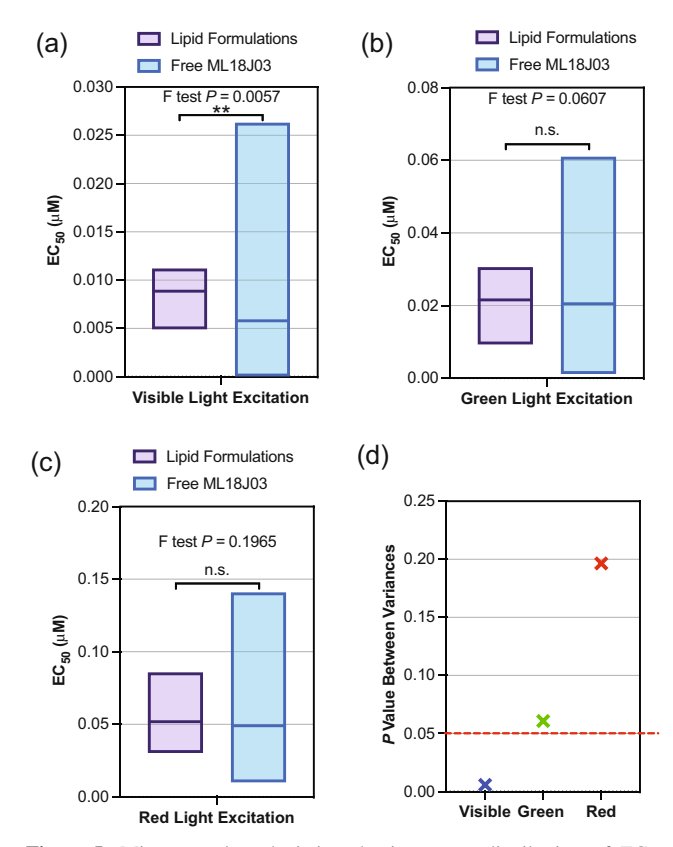


Figure 5. Min–max plots depicting the interassay distribution of EC_{50} values of free and lipid formulated ML18J03 in SK-MEL-28 human melanoma cells using visible light (a), green light (b) and red light (c) excitation. (d) The relationship between excitation light and statistical significance between variances demonstrates that lipid formulation of ML18J03 reduces interassay variability most for visible light excitation. Statistical significance between the free and lipid formulated groups was performed using a two-tailed t-test with Welch's correction and statistical significance between the variances of groups was calculated using an F test.

formulation) and decreased upon moving to the highest PS loading (84% for the 71 mol% formulation) (Table 1).

Physical and electrostatic characterization. The hydrodynamic diameters and ζ-potentials of lipo-ML18J03 and the various mic-ML18J03 formulations were characterized using dynamic light scattering (Figs. 6 and 7). Lipo-ML18J03 had a hydrodynamic diameter of 138.1 nm, which did not change significantly over an 11-day incubation period at 37°C or storage at 4°C (Fig. 6a). The hydrodynamic diameters of liposomes approved for clinical use are typically between 80 nm and 200 nm (35). Above 200 nm in diameter, liposome uptake and clearance by resident macrophages (Kupffer cells) in the liver is increased by 2–3 fold

Table 1. Entrapment efficiencies of ML18J03 in liposomal and micellar formulations.

Sample	Entrapment efficiency (%)		
lipo-ML18J03 (0.6 mol%)	93		
mic-ML18J03 (11 mol%)	100		
mic-ML18J03 (71 mol%)	84		

(36). Furthermore, large fenestrations in the blood vessels of solid tumors, along with poor lymphatic drainage, leads to increased tumor permeation and retention of nanoconstructs between 10 nm and 200 nm. As such, this range is typically considered optimal for nanoformulation-assisted drug delivery to solid tumors (37).

The polydispersity index of the lipo-ML18J03 formulation was 0.213, which also did not change significantly over the same 11-day period, suggesting that the formulation remains stable during 37°C incubation and 4°C storage (Fig. 6b). The ζpotential of the lipo-ML18J03 formulation was -1.33 mV (Table 2). The ζ-potentials of nanoconstructs significantly impact their in vitro and in vivo behavior. While cationic nanoconstructs (~30-40 mV) typically promote cell membrane association and internalization, such ζ-potentials are associated with increased clearance by the liver (38,39). While we have previously shown that anionic liposomes (~ -20 mV) significantly reduce the variability in uptake across multiple cancer cell lines, an anionic charge can also promote their uptake by macrophages by increasing opsonin binding, thereby shortening their circulation times (29,38). As such, neutral and moderately anionic ζ -potentials like those of the lipo-ML18J03 formulations are favorable.

The mic-ML18J03 formulations had a uniform size distribution between 10.2 nm and 13.2 nm in diameter, which lies within the optimal range of nanoformulation-assisted drug delivery, as described above. The ζ-potentials of the mic-ML18J03 formulations ranged from 0.21 mV to -8.11 mV. The ζ -potential of the mic-ML18J03 formulations also lie within the favorable range as described earlier. Neither the diameters nor ζ -potentials appeared to be correlated to mol% PS entrapped (Fig. 7a, Table 2), which is not unexpected as both the lipids and the PS molecules in mic-ML18J03 are neutral. It is likely that higher mol% PS entrapped in mic-ML18J03 may impact their diameters, although the data suggests that the threshold, which influences micelle size, had not been achieved at the highest mol% PS entrapment tested here (71%). The lower ML18J03 entrapment efficiencies at higher PS mol% (Table 1) suggested that the PSs may experience crowding within the micelle when the PS mol% is increased, which is supported by the quenching of ML18J03 emission at 740 nm with increasing PS mol% (Fig. 7b). To minimize self-association within the micellar structure, the ML18J03 formulation in the series with the highest emission intensity (i.e. least susceptible to emission quenching) – 11 mol% PS - was selected for the biological experiments and further characterized. The mean hydrodynamic diameter of mic-ML18J03 at 11 mol% PS was 10.2 nm and did not change significantly over 11 days in storage at 4°C or incubation at 37°C (Fig. 7c). The polydispersity indices of mic-ML18J03 at 11 mol % PS also did not change significantly over the 11 days in storage at 4°C or incubation at 37°C (Fig. 7d). Both findings suggest that the mic-ML18J03 at 11 mol% PS remains stable for up to 11 days in storage at 4°C and during incubation at 37°C.

Spectroscopy

We previously reported the spectroscopic properties of unformulated ML18J03 and proposed a photophysical model to account for its photocytotoxic effects toward cancer cells (6). The general features of the steady-state absorption and emission spectra measured for ML18J03 are qualitatively similar when formulated in liposomes (0.6 mol% PS) or micelles (11 mol% PS)

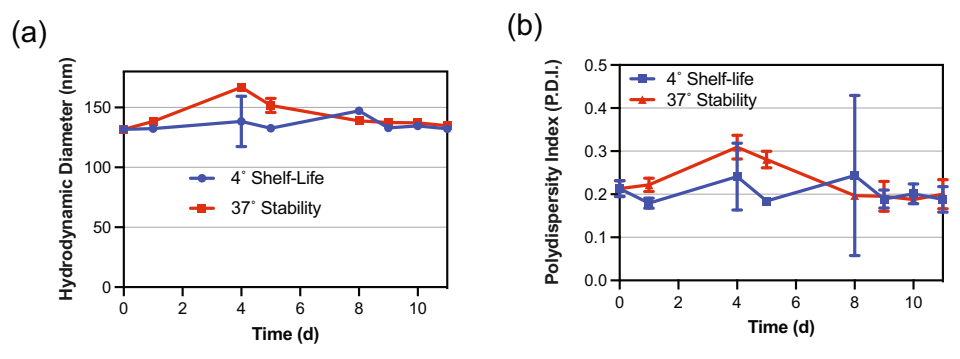


Figure 6. Hydrodynamic diameters (a) and polydispersity indices (b) of lipo-ML18J03 during storage at 4°C and incubation at 37°C for up to 11 days. Values are mean \pm SD.

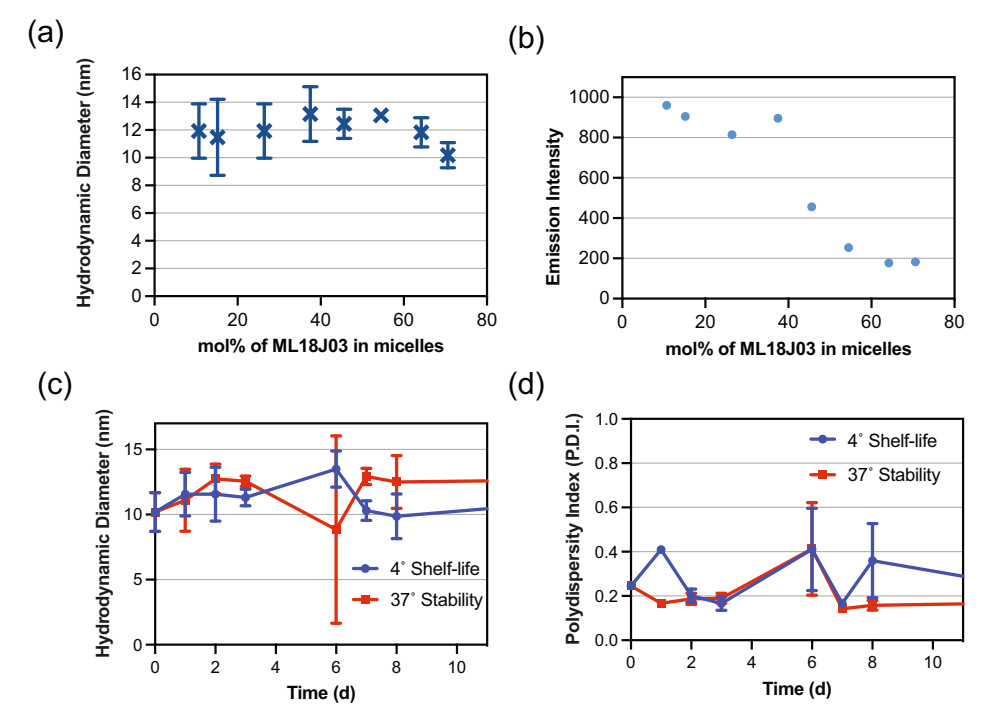


Figure 7. (a) Hydrodynamic diameters of DSPE-mPEG₂₀₀₀ micellar formulations of ML18J03 at varying mol% of the PS. Replicates were identical for the 55 mol% data point. (b) Relative emission intensities ($\lambda_{em} = 740$ nm, $\lambda_{ex} = 448$ nm) of ML18J03 formulated in micelles at varying mol% of the PS. Hydrodynamic diameters (c) and polydispersity indices (d) of mic-ML18J03 (11 mol%) in storage at 4°C and incubation at 37°C for up to 11 days. Values are mean \pm SD.

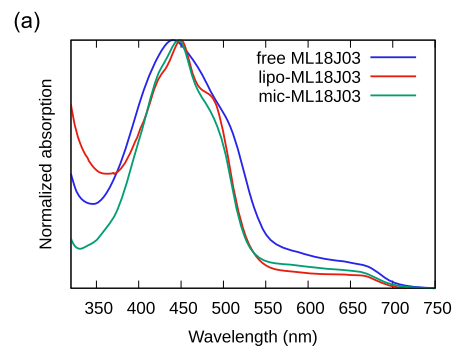
Table 2. ζ-potential measurements of lipo-ML18J03 and mic-ML18J03 at various mol% entrapment.

Formulation (ML18J03 mol%)	ζ -Potential (mean mV \pm SD)		
lipo-ML18J03 (0.6 mol%)	$-1.33~(\pm 0.48)$		
mic-ML18J03 (11 mol%)	$-2.07 (\pm 3.30)$		
mic-ML18J03 (15 mol%)	$-0.76~(\pm 0.58)$		
mic-ML18J03 (26 mol%)	$-4.98 \ (\pm 8.19)$		
mic-ML18J03 (38 mol%)	$0.21~(\pm 1.38)$		
mic-ML18J03 (46 mol%)	$-0.76 \ (\pm 0.08)$		
mic-ML18J03 (55 mol%)	$1.011~(\pm 2.18)$		
mic-ML18J03 (64 mol%)	$-4.32 (\pm 7.83)$		
mic-ML18J03 (71 mol%)	$-8.11 \ (\pm 4.80)$		

(Fig. 8, Table 3). The absorption spectra are characterized by local maxima near 450 nm that stem from overlapping longer wavelength ¹MLCT (near 490 nm) and shorter-wavelength

oligothienyl-based 1 IL/ 1 ILCT transitions (near 440 nm) (6,7), plus a broad, fairly weak absorption spanning the 550–700 nm range that arises from the formally forbidden direct 3 MLCT transitions known for Os(II) polypyridyl complexes (15). The broad, structureless emission profiles are consistent with room temperature phosphorescence from the 3 MLCT Os(d π) $\rightarrow \pi^{*}$ state. One distinguishing feature between the free and formulated ML18J03 normalized spectra is that formulation results in band sharpening. The more structured transitions for lipo- and mic-ML18J03 lead to slight shifts in the absorption and emission maxima but still falling within the 440–450 and 740–760 nm regions, respectively.

The 3 MLCT phosphorescence quantum yield of free ML18J03 in argon-sparged PBS ($\Phi_{\rm em} = 9.8 \times 10^{-5}$) is lower than its previously reported quantum yield in MeCN ($\Phi_{\rm em} = 1.1 \times 10^{-2}$) (6) that had been more thoroughly deoxygenated by freeze-pump-thaw.



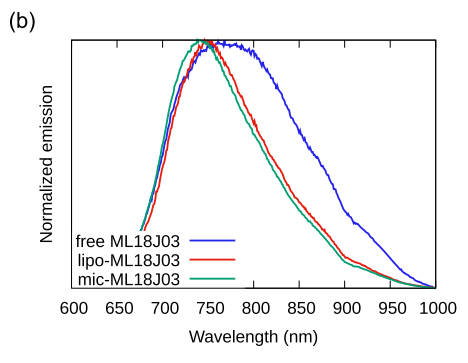


Figure 8. Comparison of the steady-state UV-vis absorption (a) and emission (b) spectra of unformulated and formulated ML18J03. Samples were prepared at 20 μm ML18J03 in PBS and argon-sparged prior to measurement. Emission spectra were collected at their excitation maxima ($λ_{ex} = 472$ nm). Lipo-ML18J03 contained 0.6 mol% PS, and mic-ML18J03 contained 11 mol% PS.

Table 3. Spectroscopic data comparing unformulated and formulated ML18J03 at 20 μ m in aqueous PBS. Steady-state emission and TA data were measured on argon-sparged samples

	λ _{abs,max} (nm)	λ _{em} (nm)	$\Phi_{ m em}$	τ _{TA} (μs)	Φ_{Δ}
Unformulated	441	761	9.8×10^{-5}		n.d.
mic-ML18J03	447	741	1.3×10^{-3}	0.70, 6.0	2.5×10^{-3}
lipo-ML18J03	449	749	1.1×10^{-3}	1.8, 6.8	3.4×10^{-3}

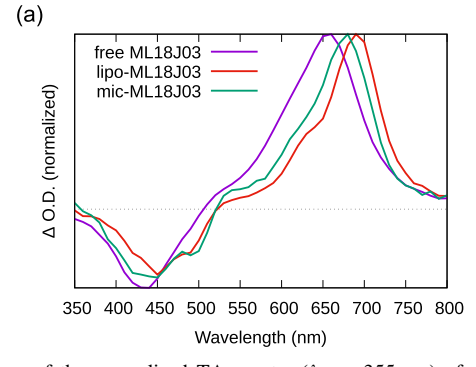
n.d., not detected.

However, lipo- and mic-ML18J03 are considerably more phosphorescent than free ML18J03 in aqueous PBS, with emission quantum yields more than an order of magnitude greater. This suggests that the lipid formulations may prevent the aggregation of free ML18J03 that leads to emission quenching. Formulation also has a positive impact on the ML18J03 $^1\mathrm{O}_2$ quantum yields (Φ_Δ) in aqueous PBS. While Φ_Δ of free, fully soluble ML18J03 in MeCN was previously determined to be 95% (6), $^1\mathrm{O}_2$ emission is not detected in aqueous PBS where ML18J03 forms aggregates. Water is an effective quencher of $^1\mathrm{O}_2$ phosphorescence (40,41), but aggregation may also suppress $^1\mathrm{O}_2$ sensitization. Small but measurable $^1\mathrm{O}_2$ production ($\Phi_\Delta\approx0.3\%$) is recovered with lipo- and mic-ML18J03, which may be due to the more hydrophobic environment of the nanolipid formulation or reduced aggregation of ML18J03 or both.

The photophysical model for ML18J03 in MeCN attributes phosphorescence to the emissive ³MLCT state and ¹O₂

sensitization primarily to the dark ³ILCT state involving the oligothienyl unit (6). The transient absorption (TA) spectra (Fig. 9a) are a superposition of both states, whereby the bleach in the 350-500 nm region has been assigned to the overlapping ground state ¹ILCT/¹MLCT transitions and the new excited state absorption (ESA) in the 550-750 nm range is the characteristic signature of the 3ILCT state and resembles that of the free oligothiophene-containing ligand. Unformulated ML18J03 in aqueous PBS produces a weak TA signal so its MeCN solution was used to generate the full differential absorption spectrum presented in Fig. 9a for comparison. The liposomal and micellar formulations produce TA signals that are qualitatively similar to those of free ML18J03 in MeCN but much more intense. The normalized spectra emphasize similar ESA signatures but with slight differences in band shapes and maxima, although such differences cannot be assigned solely to ESA since there is some overlap with the ground state bleach.

The overall photophysical model does not appear to change for lipo- and mic-ML18J03 compared to the free form; however, the kinetics are altered. The TA lifetimes for the ³ILCT state were measured at 660 nm for free and formulated ML18J03 in aqueous PBS, where it was possible to collect the decay for the weak ESA of free ML18J03 in PBS by single-wavelength parameter optimization and averaging the signal over a large number of transients. Lipid formulation produced average ³ILCT lifetimes that were longer than those of the free ML18J03 in the same solvent (Fig. 9b). The decays were biexponential, as observed for free ML18J03, but with both short and long



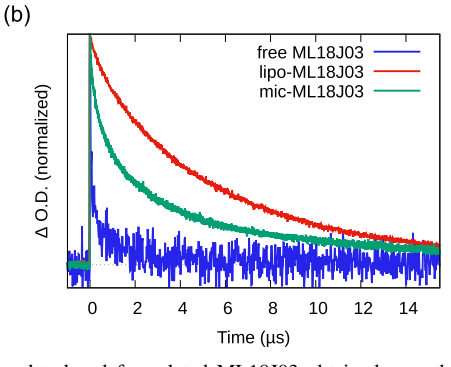


Figure 9. Comparison of the normalized TA spectra ($λ_{ex} = 355$ nm) of unformulated and formulated ML18J03 obtained over the first 5 μs following the excitation pulse (a). Normalized TA decay signals measured at 660 nm (b). Samples contained 20 μm ML18J03 in argon-sparged PBS except for free ML18J03 in (a), which was collected in argon-sparged MeCN due to its extremely weak TA signal in PBS solution.

components prolonged. The lifetimes for unformulated ML18J03 were $\tau_1 = 0.16 \,\mu s$ and $\tau_2 = 1.5 \,\mu s$. The prolonged components for lipo- and mic-ML18J03 were $\tau_1 = 0.70 \,\mu\text{s}$, $\tau_2 = 6.0 \,\mu\text{s}$ and $\tau_1 = 1.8 \,\mu\text{s}, \, \tau_2 = 7.8 \,\mu\text{s}, \, \text{respectively}.$ Given that the ³ILCT state is preferentially implicated in ¹O₂ production and thus photocytotoxicity, the greater intensities and longer lifetimes of its transients for lipo- and mic-ML18J03 suggest that formulation enhances the desirable photophysical properties of aqueous ML18J03 possibly through suppressed aggregation. Whether these photophysical profiles are improved for cellular ML18J03 is not known definitively, but the reduced variance in photocytotoxicity for formulated ML18J03 led to average EC50 values that fell at the more potent end of the much wider unformulated range. This suggests that formulation may result in improved photophysical properties in the cellular environment.

DISCUSSION

It is well established that lipid formulations are effective and clinically translatable platforms for improving the solubility of hydrophobic PS molecules. In this study, we show that formulating the hydrophobic normoxia- and hypoxia-active Os PS, ML18J03, in liposomes and micelles improves its solubility. Formulation prevents the aggregation and sedimentation of ML18J03 that contributes to the broad interassay variability in phototherapeutic response. The result is a more robust and predictable PDT response that is more consistent across multiple assay repeats. This robustness is valuable for improving the reliability of reporting on the phototherapeutic efficacies of novel hydrophobic metal-based PSs, such as ML18J03. Ultimately, lipid formulation of ML18J03 will also improve its solubility in serum, its pharmacokinetic profile and the robustness of its in vivo phototherapeutic response. Future in vivo work evaluating the circulation half-lives, bulk tumor delivery and tumor penetration will be conducted to compare the liposomal and micellular formulations of ML18J03. Furthermore, as the lipid load can also contribute to systemic toxicity of the liposomal and micellular carriers, comprehensive dose-limiting toxicity studies of the liposomal and micellular formulations of ML18J03 will be assessed to determine the optimal formulation for in vivo PDT. These lipid formulations address a significant hurdle in being able to rigorously evaluate novel hydrophobic metal-based PSs and promise to expedite their full in vivo evaluation to maximize their unique therapeutic benefits, including hypoxia activity.

Acknowledgements-The technical assistance of Pariya Zare is gratefully acknowledged. Funding from the National Institutes of Health, National Cancer Institute for G.O. is also gratefully acknowledged (R00CA215301). S.A.M. and C.G.C. thank the National Cancer Institute (NCI) of the National Institutes of Health (NIH) (Award R01CA222227) for support. The content in this work is solely the responsibility of the authors and does not necessarily represent the official views of the National Institutes of Health.

CONFLICTS OF INTEREST

S.A.M. has a potential research conflict of interest due to a financial interest with Theralase Technologies, Inc. and PhotoDynamic, Inc. A management plan has been created to preserve objectivity in research in accordance with UTA policy.

SUPPORTING INFORMATION

Additional supporting information may be found online in the Supporting Information section at the end of the article:

Figure S1. Spectral output of the light sources used in the photobiological experiments. All light sources were LEDs except for the 733 nm laser light.

Table S1. Interassay performance: cytotoxicity and photocytotoxicity of ML18J03 toward normoxic-treated (~18.5% O2) SK-MEL-28 melanoma cells.

Table S2. Interassay performance: cytotoxicity and photocytotoxicity of ML18J03 toward hypoxic-treated (1% O2) SK-MEL-28 melanoma cells.

Table S3. Standard dilutions used for in vitro experiments in a deep well plate.

Table S4. Extra dilutions used for in vitro experiments in a deep well plate, used for testing carry-over effect.

Table S5. Interassay performance: cytotoxicity and photocytotoxicity of liposomal ML18J03 toward normoxic-treated (~18.5% O2) SK-MEL-28 melanoma cells.

REFERENCES

- 1. Celli, J. P., B. Q. Spring, I. Rizvi, C. L. Evans, K. S. Samkoe, S. Verma, B. W. Pogue and T. Hasan (2010) Imaging and Photodynamic therapy: Mechanisms, monitoring, and optimization. Chem. Rev. 110(5), 2795-2838.
- 2. Santos, L. L., J. Oliveira, E. Monteiro, J. Santos and C. Sarmento (2018) Treatment of head and neck cancer with Photodynamic therapy with Redaporfin: A clinical case report. Case Rep. Oncol. 11(3), 769-776.
- 3. Abdel-Hady, E. S., P. Martin-Hirsch, M. Duggan-Keen, P. L. Stern, J. V. Moore, G. Corbitt, H. C. Kitchener and I. N. Hampson (2001) Immunological and viral factors associated with the response of Vulval intraepithelial neoplasia to Photodynamic therapy. Cancer Res. **61**(1), 192–196.
- 4. Kabingu, E., A. R. Oseroff, G. E. Wilding and S. O. Gollnick (2009) Enhanced systemic immune reactivity to a basal cell carcinoma associated antigen following Photodynamic therapy. Clin. Cancer Res. 15(13), 4460-4466.
- 5. Ghosh, P., Y. Hanada, B. Linn, T. Mangels-Dick, B. Roy and K. Wang (2021) S1479 abscopal effect of Intratumoral Photodynamic therapy is associated with increased tumor directed T cells. Am. J. Gastroenterol. 116(1), S676-S677.
- 6. Roque, J. A., III, P. C. Barrett, H. D. Cole, L. M. Lifshits, G. Shi, S. Monro, D. von Dohlen, S. Kim, N. Russo, G. Deep, C. G. Cameron, M. E. Alberto and S. A. McFarland (2020) Breaking the barrier: An osmium photosensitizer with unprecedented hypoxic phototoxicity for real world Photodynamic therapy. Chem. Sci. 11, 9784-9806.
- 7. Roque, J. A., P. C. Barrett, H. D. Cole, L. M. Lifshits, E. Bradner, G. Shi, D. von Dohlen, S. Kim, N. Russo, G. Deep, C. G. Cameron, M. E. Alberto and S. A. McFarland (2020) Os(II) Oligothienyl complexes as a hypoxia-active photosensitizer class for Photodynamic therapy. *Inorg. Chem.* **59**(22), 16341–16360.
- 8. Roque, J. A., III, H. D. Cole, P. C. Barrett, L. M. Lifshits, R. O. Hodges, S. Kim, G. Deep, A. Francés-Monerris, M. E. Alberto, C. G. Cameron and S. A. McFarland (2022) Intraligand excited states turn a ruthenium oligothiophene complex into a light-triggered Ubertoxin with anticancer effects in extreme hypoxia. J. Am. Chem. Soc. **144**(18), 8317-8336.
- 9. Cole, H. D., J. A. Roque, G. Shi, L. M. Lifshits, E. Ramasamy, P. C. Barrett, R. O. Hodges, C. G. Cameron and S. A. McFarland (2022) Anticancer agent with inexplicable potency in extreme hypoxia: Characterizing a light-triggered ruthenium Ubertoxin. J. Am. Chem. Soc. 144(22), 9543-9547.

- 10. Konda, P., L. M. Lifshits, J. A. Roque, H. D. Cole, C. G. Cameron, S. A. McFarland and S. Gujar (2021) Discovery of immunogenic cell death-inducing ruthenium-based photosensitizers for anticancer Photodynamic therapy. OncoImmunology 10(1), 1863626.
- 11. Konda, P., J. A. Roque III, L. M. Lifshits, A. Alcos, E. Azzam, G. Shi, C. G. Cameron, S. A. McFarland and S. A. Gujar (2022) Photodynamic therapy of melanoma with new, structurally similar, NIRabsorbing ruthenium (II) complexes promotes tumor growth control via distinct hallmarks of immunogenic cell death. Am. J. Cancer Res. 12, 210-228.
- 12. Lifshits, L. M., J. A. Roque III, P. Konda, S. Monro, H. D. Cole, D. von Dohlen, S. Kim, G. Deep, R. P. Thummel, C. G. Cameron, S. Gujar and S. A. McFarland (2020) Near-infrared absorbing Ru(II) complexes act as Immunoprotective Photodynamic therapy (PDT) agents against aggressive melanoma. Chem. Sci. 11(43), 11740-11762.
- 13. Monro, S., K. L. Colón, H. Yin, J. Roque, P. Konda, S. Gujar, R. P. Thummel, L. Lilge, C. G. Cameron and S. A. McFarland (2019) Transition metal complexes and Photodynamic therapy from a tumor-centered approach: Challenges, opportunities, and highlights from the development of TLD1433. Chem. Rev. 119(2), 797-828.
- 14. McFarland, S. A., A. Mandel, R. Dumoulin-White and G. Gasser (2020) Metal-based photosensitizers for Photodynamic therapy: The future of multimodal oncology? Curr. Opin. Chem. Biol. 56, 23-27.
- 15. Decurtins, S., F. Felix, J. Ferguson, H. U. Guedel and A. Ludi (1980) The electronic Spectrum of tris(2,2'-bipyridine)iron(2+) and tris (2,2'-bipyridine)osmium(2+). J. Am. Chem. Soc. **102**(12), 4102-4106.
- 16. Obaid, G., M. Broekgaarden, A.-L. Bulin, H.-C. Huang, J. Kuriakose, J. Liu and T. Hasan (2016) Photonanomedicine: A convergence of Photodynamic therapy and nanotechnology. Nanoscale 8 (25), 12471-12503.
- 17. Mellish, K. J. and S. B. Brown (2001) Verteporfin: A milestone in Opthalmology and Photodynamic therapy. Expert. Opin. Pharmacother. 2(2), 351-361.
- 18. Gaio, E., D. Scheglmann, E. Reddi and F. Moret (2016) Uptake and photo-toxicity of Foscan®, Foslip® and Fospeg® in multicellular tumor spheroids. J. Photochem. Photobiol. B 161, 244-252.
- 19. Bovis, M. J., J. H. Woodhams, M. Loizidou, D. Scheglmann, S. G. Bown and A. J. MacRobert (2012) Improved in vivo delivery of M-THPC via pegylated liposomes for use in Photodynamic therapy. J. Control. Release 157(2), 196-205.
- 20. Petri, A., D. Yova, E. Alexandratou, M. Kyriazi and M. Rallis (2012) Comparative characterization of the cellular uptake and Photodynamic efficiency of Foscan® and Fospeg in a human prostate cancer cell line. Photodiagn. Photodyn. Ther. 9(4), 344-354.
- 21. Rubtsova, N. I., M. C. Hart, A. D. Arroyo, S. A. Osharovich, B. K. Liebov, J. Miller, M. Yuan, J. M. Cochran, S. Chong, A. G. Yodh, T. M. Busch, E. J. Delikatny, N. Anikeeva and A. V. Popov (2021) NIR fluorescent imaging and Photodynamic therapy with a novel Theranostic phospholipid probe for triple-negative breast cancer cells. Bioconjug. Chem. 32(8), 1852-1863.
- 22. Pedroso, A., F. de Morais, R. Sonchini Gonçalves, K. Souza Campanholi, B. Martins de França, O. Augusto Capeloto, D. Lazarin-Bidoia, R. Bento Balbinot, C. Vataru Nakamura, L. Carlos Malacarne, W. Caetano and N. Hioka (2021) Photophysical characterization of hypericin-loaded in micellar, liposomal and copolymer-lipid nanostructures based F127 and DPPC liposomes. Spectrochim. Acta A Mol. Biomol. Spectrosc. 248, 119173.
- 23. Sibata, M. N., A. C. Tedesco and J. M. Marchetti (2004) Photophysicals and Photochemicals studies of zinc(II) phthalocyanine in long time circulation micelles for Photodynamic therapy use. Eur. J. Pharm. Sci. 23(2), 131-138.
- 24. Cabral, H., Y. Matsumoto, K. Mizuno, Q. Chen, M. Murakami, M. Kimura, Y. Terada, M. R. Kano, K. Miyazono, M. Uesaka, N. Nishiyama and K. Kataoka (2011) Accumulation of Sub-100 nm polymeric micelles in poorly permeable Tumours depends on size. Nat. Nanotechnol. 6(12), 815-823.
- 25. Matsumura, Y. and K. Kataoka (2009) Preclinical and clinical studies of anticancer agent-incorporating polymer micelles. Cancer Sci. 100(4), 572-579.

- 26. Liu, Y., L. Scrivano, J. D. Peterson, M. H. A. M. Fens, I. B. Hernández, B. Mesquita, J. S. Toraño, W. E. Hennink, C. F. van Nostrum and S. Oliveira (2020) EGFR-targeted nanobody functionalized polymeric micelles loaded with MTHPC for selective Photodynamic therapy. Mol. Pharm. 17(4), 1276-1292.
- 27. Tsukioka, Y., Y. Matsumura, T. Hamaguchi, H. Koike, F. Moriyasu and T. Kakizoe (2002) Pharmaceutical and biomedical differences between micellar doxorubicin (NK911) and liposomal doxorubicin (Doxil). Jpn. J. Cancer Res. 93(10), 1145-1153.
- Wakaskar, R. R. (2018) General overview of lipid-polymer hybrid nanoparticles, dendrimers, micelles, liposomes, Spongosomes and Cubosomes. J. Drug Target. 26(4), 311-318.
- Obaid, G., S. Bano, S. Mallidi, M. Broekgaarden, J. Kuriakose, Z. Silber, A.-L. Bulin, Y. Wang, Z. Mai, W. Jin, D. Simeone and T. Hasan (2019) Impacting pancreatic cancer therapy in heterotypic in vitro organoids and in vivo tumors with specificity-tuned, NIRactivable Photoimmunonanoconjugates: Towards conquering desmoplasia? Nano Lett. 19(11), 7573-7587.
- Obaid, G., S. Bano, H. Thomsen, S. Callaghan, N. Shah, J. W. R. Swain, W. Jin, X. Ding, C. G. Cameron, S. A. McFarland, J. Wu, M. Vangel, S. Stoilova-McPhie, J. Zhao, M. Mino-Kenudson, C. Lin and T. Hasan (2022) Remediating desmoplasia with EGFR-targeted photoactivable multi-inhibitor liposomes doubles overall survival in pancreatic cancer. Adv. Sci. 9, 2104594.
- Spring, B. Q., R. Bryan Sears, L. Z. Zheng, Z. Mai, R. Watanabe, M. E. Sherwood, D. A. Schoenfeld, B. W. Pogue, S. P. Pereira, E. Villa and T. Hasan (2016) A photoactivable multi-inhibitor nanoliposome for tumour control and simultaneous inhibition of treatment escape pathways. Nat. Nanotechnol. 11(4), 378-387.
- 32. Guirguis, M., C. Bhandari, J. Li, M. Eroy, S. Prajapati, R. Margolis, N. Shrivastava, K. Hoyt, T. Hasan and G. Obaid (2021) Membrane composition is a functional determinant of NIR-Activable liposomes in orthotopic head and neck cancer. Nano 10(12), 3169-3185.
- Obaid, G., W. Jin, S. Bano, D. Kessel and T. Hasan (2019) Nanolipid formulations of benzoporphyrin derivative: Exploring the dependence of Nanoconstruct Photophysics and photochemistry on their therapeutic index in ovarian cancer cells. Photochem. Photobiol. 95(1), 364-377.
- 34. Yang, Q., K. R. Moulder, M. S. Cohen, S. Cai and L. M. Forrest (2015) Cabozantinib loaded DSPE-PEG2000 micelles as delivery system: Formulation, characterization and cytotoxicity evaluation. BAOJ Pharm. Sci. 1, 001.
- 35. Bulbake, U., S. Doppalapudi, N. Kommineni and W. Khan (2017) Liposomal formulations in clinical use: An updated review. Pharmaceutics 9(4), 12.
- 36. Kamps, J. A. A. M., H. W. M. Morselt, P. J. Swart, D. K. F. Meijer and G. L. Scherphof (1997) Massive targeting of liposomes, surfacemodified with Anionized albumins, to hepatic endothelial cells. Proc. Natl. Acad. Sci. 94(21), 11681-11685.
- Kalyane, D., N. Raval, R. Maheshwari, V. Tambe, K. Kalia and R. K. Tekade (2019) Employment of enhanced permeability and retention effect (EPR): Nanoparticle-based precision tools for targeting of therapeutic and diagnostic agent in cancer. Mater. Sci. Eng. C 98, 1252-1276.
- 38. Zelphati, O., L. S. Uyechi, L. G. Barron and F. C. Szoka (1998) Effect of serum components on the Physico-chemical properties of cationic lipid/oligonucleotide complexes and on their interactions with cells. Biochim. Biophys. Acta BBA - Lipids Lipid Metab. 1390 (2), 119-133.
- 39. Krasnici, S., A. Werner, M. E. Eichhorn, M. Schmitt-Sody, S. A. Pahernik, B. Sauer, B. Schulze, M. Teifel, U. Michaelis, K. Naujoks and M. Dellian (2003) Effect of the surface charge of liposomes on their uptake by angiogenic tumor vessels. Int. J. Cancer 105(4), 561-567
- 40. DeRosa, M. C. and R. J. Crutchley (2002) Photosensitized singlet oxygen and its applications. Coord. Chem. Rev. 233-234, 351-371.
- 41. Ogilby, P. R. and C. S. Foote (1983) Chemistry of Singlet Oxygen. 42. Effect of solvent, solvent isotopic substitution, and temperature on the lifetime of singlet molecular oxygen. J. Am. Chem. Soc. 105 (11), 3423-3430.